A Numerical Study of Near Inertial Motions in Mid-Atlantic Bight Area Induced by Hurricane Irene (2011)

Peida Han[1] and Xiping Yu[2]

Abstract

Hurricane Irene generated strong near inertial currents (NICs) in the ocean waters when passing over the Mid-Atlantic Bight (MAB) of the U. S. East Coast in late August 2011. It is demonstrated that a combination of the valuable field data with detailed model results can be taken advantage to study the development and decay mechanism of this event. Numerical results obtained with regional oceanic modeling system (ROMS) are shown to agree well with the field data. Both computed and observed results show that the NICs were significant in most areas of the MAB region except in the nearshore area where the stratification was totally destroyed by the hurricane-induced strong mixing. Based on the energy budget, it is clarified that the near inertial kinetic energy (NIKE) was mainly gained from the wind power during the hurricane event. In the deep water region, NIKE was basically balanced by the vertical turbulence diffusion (40%) and downward divergence (33%). While in the continental shelf region, NIKE was mainly dissipated by the vertical turbulence diffusion (67%) and partially by the bottom friction (24%). Local dissipation of NIKE due to turbulence diffusion is much more closely related to the rate of the vertical shear rather than the intensity of turbulence. The strong vertical shear at the offshore side of the continental shelf leaded to a rapid dissipation of NIKE in this region.

Keywords: Hurricane Irene (2011); Mid-Atlantic Bight; Near inertial current; Energy budget; Timescale of near inertial energy decay

---

[1] PhD Candidate. Department of Hydraulic Engineering, Tsinghua University, Beijing, China.

[2] Corresponding Author. Professor. Department of Ocean Science and Engineering, Southern University of Science and Technology, Shenzhen, China. Email: yuxp@sustech.edu.cn

1. Introduction

Near inertial currents (NICs), observed widely in ocean basins around the world, are characterized by the important role of Coriolis effect and by the periodic motion with the frequency of an inertial mode (Garrett, 2001). The basic energy source of these freely flowing currents is the wind power (Pollard, 1980; D'Asaro et al., 1985). Globally, the annually averaged wind power supply to NICs was estimated ranging from 0.3 TW to more than 1 TW by previous investigators (Alford, 2003a; Furuichi et al., 2008; Rimac et al., 2013). As a comparison, the total power required to maintain the abyssal stratification and the thermohaline circulation is about 2 TW (Munk and Wunsch, 1998). This implies that NIC is a very important phenomenon in physical oceanography (Gregg, 1987; Alford, 2003b; Jochum et al., 2013).

A tropical or an extratropical cyclone (hereinafter collectively referred as TC) is a rotating low-pressure and strong-wind mesoscale weather system, which generates NICs more powerfully than other types of atmospheric processes in nature (Alford et al., 2016; Steiner et al., 2017). When a TC passes over a deep ocean, enormous energy is directly transferred into the ocean waters, which rapidly generates strong NICs with a velocity up to 1 m/s in the horizontal direction of the mixed layer (Price, 1983; Sanford et al., 2011). Right-bias effect is often shown in the NIC pattern, i.e., NICs are more intense on the right side of the hurricane track, due to the resonance between the surface flow driven by NICs and clockwise rotating wind stress on the right side (Chang and Anthes, 1978; Price, 1994). After the passage of a TC, the surface near inertial energy usually persists for several inertial cycles, and then gradually decays (Price, 1983; Sanford et al., 2011; Hormann et al., 2014; Zhang et al., 2016; Wu et al., 2020).

It is known that NICs in shallow waters show some significant differences with those in deep waters and the velocity of NICs in shallow waters is usually of a smaller magnitude of 0.1-0.5 m/s (Chen and Xie, 1997; Rayson et al., 2015; Yang et al., 2015; Chen et al., 2017; Zhang et al., 2018). The decrease of current velocity in shallow waters may be an effect of the sea-bottom friction as Rayson et al. (2015) pointed out. Chen and Xie (1997), however,

found that it was because a significant part of the wind input, which may otherwise be an energy source of the NICs, was exhausted to generate a wave-induced nearshore current system. Chen et al. (2017) considered that barotropic waves in the shallow waters, such as seiches, may trap some wind energy. In addition to the difference in magnitude, the modes of the NICs in shallow and deep waters are also different. More specifically, a two-layer structure was observed in shallow waters in several studies, i.e., NICs were in opposite phases in surface and bottom layers, which differed from the conventional multi-layer mode in deep waters (Chen et al., 1996; Shearman, 2005; Yang et al., 2015), though a multi-layer mode may also be observed sometimes in nearshore waters due to combined effect of changing wind stress, variable stratification and nonlinear bottom friction (Mackinnon and Gregg, 2005).

There have been a considerable number of studies on the decay of specific TC generated NICs in coastal regions. Rayson et al. (2015) paid attention to four intense TCs on the Australian North-West Shelf and related the rapid decay of NICs in shallow waters to the bottom friction. Yang et al. (2015) examined coastal ocean responses to Typhoon Washi and found that the negative background vorticity could trap near inertial energy and result in a slow decay. Shen et al. (2017) investigated five TCs over the Taiwan Strait and identified a rapid decaying rate due to nonlinear interaction between NICs and tides. Zhang et al. (2018) studied Hurricane Arthur in Mid-Atlantic Bight and showed that excessive wind input does not necessarily lead to amplification of NICs because intensive wind input is usually accompanied by an even higher rate of energy dissipation.

Though a significant number of investigations have been conducted, some basic features of a TC induced NIC in the coastal ocean are still not clarified. For instance, the energy budget in the NIC generated by a TC has not yet been thoroughly discussed in either deep or shallow waters; and the relative importance of different physical processes including advection, conversion, turbulence diffusion, bottom friction, energy divergence, etc., in the energy budget has not yet been fully understood. In addition, it is still not concluded on which processes dominate the decay of near inertial energy or on how each physical process

affects the decay rate of the near inertial energy in deep and shallow waters, respectively. Our limited understanding to the basic features of a TC induced NIC is largely due to the difficulties in ocean observations under extreme weather.
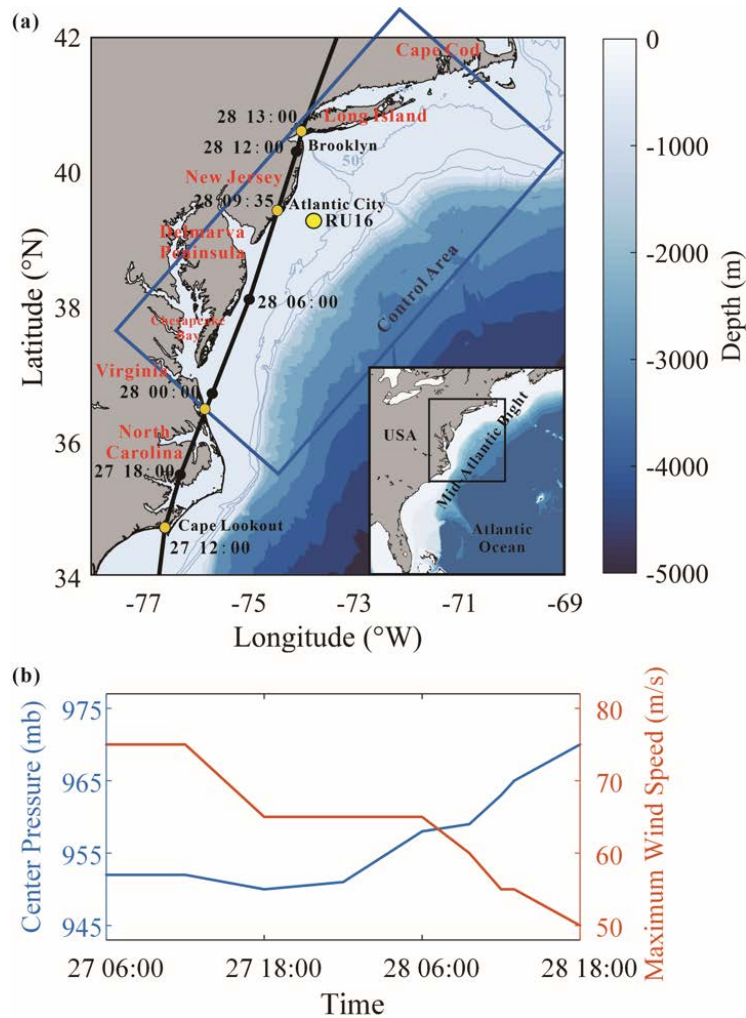
Figure 1. (a) Map of the MAB region. Best track of Hurricane Irene (2011) reported by Avila and Cangialosi (2011) is shown by a black line. Reanalysis data provided by H*WIND shows a similar track with Avila and Cangialosi (2011) and is thus omitted. The mean position of Glider RU16 is marked by a yellow circle. The control domain defined in Section 4 is marked by a blue box. (b) Time series of center pressure and 10-m maximum wind speed of Hurricane Irene reported by Avila and Cangialosi (2011).

In this study, we pay a close attention to the NIC induced by Hurricane Irene (2011). Hurricane Irene (2011) crossed over the Mid-Atlantic Bight (MAB), a coastal region of the North Atlantic, extending from Cape Cod, Massachusetts to Cape Lookout, North Carolina,

94 USA, as shown in Figure 1a. Before the hurricane event, seawater stratification in MAB

95 was quite strong due to the Cold Pool effect (Lentz, 2017) and the temperature difference

96 between the surface and the bottom exceeded 10 °C. The vertical gradient of the temperature

97 should also be very large because previous studies showed that the thermocline in shelf

98 region was rather thin; for instance, the thermocline was less than 5 m in the place where

99 water depth was around 40 m (Glenn et al., 2016; Seroka et al., 2017). During the passage

100 of Hurricane Irene (2011), a network of High-frequency (HF) radars measured the surface

101 currents in MAB (Roarty et al., 2010). Meanwhile, a Slocum glider launched near New

102 Jersey measured the vertical profiles of the temperature and the salinity (Schofield et al.,

103 2010). Combination of the valuable field data with effective numerical techniques then

104 provided an opportunity to achieve a comprehensive study of the NICs generated by this

105 hurricane event.

106 **2. Numerical Model**

107 2.1 Basic Equations

108   In this study, the ocean responses to Hurricane Irene (2011) are studied using the

109 regional oceanic modeling system (ROMS) (Shchepetkin and McWilliams, 2005;

110 Haidvogel et al., 2008). ROMS deals with the Reynolds-averaged N-S equations in the σ

111 coordinate system (Freeman et al., 1972). Specifically, the Cartesian coordinate z is

112 replaced by σ based on a general relation $\chi(\sigma) = (z - \eta)/D$, where η is the vertical

113 displacement of the free surface and D is the instantaneous water depth, while $\chi(\sigma)$ is

114 a stretching function introduced for grid refinement. In the σ-coordinate system the

115 Reynolds-averaged N-S equations may finally be expressed as

116
$$\frac{\partial \xi}{\partial t} + \frac{\partial(\xi u)}{\partial x} + \frac{\partial(\xi v)}{\partial y} + \frac{\partial(\xi \omega)}{\partial \sigma} = 0 \tag{1}$$

117
$$\frac{\partial\left(\xi u\right)}{\partial t}+\frac{\partial\left(\xi uu\right)}{\partial x}+\frac{\partial\left(\xi uv\right)}{\partial y}+\frac{\partial\left(\xi u\omega\right)}{\partial\sigma}-f\xi v+\frac{\xi}{\rho}\frac{\partial p}{\partial x}$$
$$=-g\xi\left(\chi\frac{\partial D}{\partial x}+\frac{\partial\eta}{\partial x}\right)+\frac{\partial}{\partial\sigma}\left(\frac{\nu}{\xi}\frac{\partial u}{\partial\sigma}\right)+\frac{\partial}{\partial x}\left(\xi\nu'\frac{\partial u}{\partial x}\right)+\frac{\partial}{\partial y}\left(\xi\nu'\frac{\partial u}{\partial y}\right) \quad (2)$$

118
$$\frac{\partial\left(\xi v\right)}{\partial t}+\frac{\partial\left(\xi uv\right)}{\partial x}+\frac{\partial\left(\xi vv\right)}{\partial y}+\frac{\partial\left(\xi v\omega\right)}{\partial\sigma}+f\xi u+\frac{\xi}{\rho}\frac{\partial p}{\partial y}$$
$$=-g\xi\left(\chi\frac{\partial D}{\partial y}+\frac{\partial\eta}{\partial y}\right)+\frac{\partial}{\partial\sigma}\left(\frac{\nu}{\xi}\frac{\partial v}{\partial\sigma}\right)+\frac{\partial}{\partial x}\left(\xi\nu'\frac{\partial v}{\partial x}\right)+\frac{\partial}{\partial y}\left(\xi\nu'\frac{\partial v}{\partial y}\right) \quad (3)$$

119
$$0=-\frac{1}{\rho}\frac{\partial p}{\partial\sigma}-g\xi \quad (4)$$

120
$$\frac{\partial\left(\xi C\right)}{\partial t}+\frac{\partial\left(\xi uC\right)}{\partial x}+\frac{\partial\left(\xi vC\right)}{\partial y}+\frac{\partial\left(\xi\omega C\right)}{\partial\sigma}$$
$$=\frac{\partial}{\partial\sigma}\left(\frac{\kappa}{\xi}\frac{\partial C}{\partial\sigma}\right)+\frac{\partial}{\partial x}\left(\xi\kappa'\frac{\partial C}{\partial x}\right)+\frac{\partial}{\partial y}\left(\xi\kappa'\frac{\partial C}{\partial y}\right) \quad (5)$$

121 where, $\xi=\partial z/\partial\sigma=D\left(\partial\chi/\partial\sigma\right)$; u, v, ω are the velocity components in x, y, σ

122 directions, respectively; C stands for the potential temperature T or salinity S; p is

123 the seawater pressure; ρ is the density of the seawater; $f=2\Omega\sin\phi$ is the Coriolis

124 parameter with $2\Omega=1.458\times10^{-4}$ s^{-1} and ϕ being the latitude; ν and κ are the

125 diffusion coefficients for momentum and potential temperature or salinity, respectively, in

126 the vertical direction; ν' and κ' are those in the horizontal directions; Note that Eq. (1)

127 is the continuity equation; Eqs. (2) and (3) are equations of motion in two horizontal

128 directions; Eq. (4) is the hydrostatic assumption; Eq. (5) is the advection-diffusion equation

129 of the potential temperature or the salinity. The density of the seawater ρ is determined

130 following the equation of state proposed by Jackett and McDougall (1995):

131
$$\rho\left(S,T,p\right)=\frac{\rho_0}{1-p/K\left(S,T,p\right)} \quad (6)$$

132 where $\rho_0=\rho\left(S,T,0\right)$ is the seawater density at the standard atmospheric pressure and

133 $K\left(S,T,p\right)$ is the bulk modulus, both are given by Jackett and McDougall (1995).

134   The vertical mixing is known to play an important role in determining the structure of

135 a NIC, so it must be properly evaluated. In this study, we consider $\nu=\nu_0+\nu_e$ and

136     $\kappa = \kappa_0 + \kappa_e$, in which ν_0 and κ_0 are the molecular viscosity and diffusivity of the

137   seawater, set to $\nu_0 = 10^{-5}\,\mathrm{m^2/s}$ and $\kappa_0 = 10^{-6}\,\mathrm{m^2/s}$ following previous suggestions (Xu

138   et al., 2002; Li and Zhong, 2007; Lentz, 2017), while ν_e and κ_e are the eddy viscosity

139   and diffusivity, determined by the conventional k-ε turbulence model (see Rodi (1987) and

140   Umlauf and Burchard (2003) for detailed description), a widely employed model that

141   demonstrated good performance in simulating various oceanographic processes

142   (Olabarrieta et al., 2011; Toffoli et al., 2012; Zhang et al., 2018).

143   Horizontal mixing is included in Eqs. (2), (3) and (5), though it has been pointed out

144   to play a relatively insignificant role in simulating response of the stratified ocean to a

145   hurricane, as compared to vertical mixing (Li and Zhong, 2007; Zhai et al., 2009; Dorostkar

146   et al., 2010). In the ocean basin of the present interest, the horizontal diffusion coefficient

147   was estimated to be an order of 10 $\mathrm{m^2/s}$ under extreme conditions, e.g., TC condition

148   (Allahdadi, 2014; Mulligan and Hanson, 2016). Thus, we take $\nu' = \kappa' = 10\,\mathrm{m^2/s}$ in the

149   present study for simplicity to simulate the ocean response to Hurricane Irene.

2.2 Computational Conditions

151   In order to fully capture the NIC induced by Hurricane Irene (2011), our computational

152   domain covers the entire MAB regions of the U. S. East Coast extending from Cape Cod,

153   Massachusetts, to Cape Lookout, North Caroline. The computational domain is discretized

154   into 35 layers with refinement near the surface and covered with a 5 km×5 km grid in the

155   horizontal plane. The 1 arc-min bathymetry data is obtained from ETOPO1 Global Relief

156   Model (Amante and Eakins, 2009) and resampled to a resolution of 5 km. The simulation

157   starts from 20 August, one week before the hurricane event and lasted for a period of 16

158   days. The time step is set to 1 min.

159   The initial and open boundary conditions of the seawater temperature and salinity, the

160   ocean flow velocities and the sea surface elevation are all from the Hybrid Coordinate Ocean

161   Model (HYCOM, https://www.hycom.org/) with a resolution of 1/12° in space and 3 hr in

162   time (Cummings, 2005; Chassignet et al., 2007). The initial stratification in the HYCOM is

163   examined through a comparison with the 4D data provided by Experimental System for

164   Predicting Shelf and Slope Optics (ESPreSSO, http://www.myroms.org/espresso/). Seven

165   tidal constitutes (M2, S2, N2, K2, O1, K1, Q1) included in the simulation are derived from

166   the ADvanced CIRCulation model (ADCIRC, https://adcirc.org/). Daily inflows from the

167   eleven largest rivers, containing Susquehanna River, Delaware River, Hudson River,

168   Potomac River, etc., are obtained from the United States Geological Survey (USGS,

169   https://waterdata.usgs.gov/). The so-called radiation-nudging condition is adopted at the

170   open boundaries (Marchesiello et al., 2001). Wet-and-dry option is activated at coastal

171   boundaries (Warner et al., 2013). The seabed boundary condition is required to satisfy:

172

$$\nu \frac{\partial \mathbf{u}}{\partial z} = \boldsymbol{\tau}_{\mathrm{b}} = \rho \left[\frac{\lambda}{\ln\left(\Delta z \, / \, z_{0}\right)} \right]^{2} \left| \mathbf{u}_{\mathrm{b}} \right| \mathbf{u}_{\mathrm{b}} \tag{7}$$

173   where, $\boldsymbol{\tau}_{\mathrm{b}}$ is the bottom friction; λ is the von Karman constant; $\mathbf{u}_{\mathrm{b}}$ is the fluid velocity

174   at the center of the bottom layer; Δz is the distance between the center of the bottom layer

175   and the seabed; z_{0} is the bottom roughness, which is set to 0.02 m in MAB following

176   Churchill et al. (1994).

177   The hurricane wind forcing required in this study can be obtained from two sources,

178   i.e., the H*WIND data, with a spatial resolution of 6 km and a temporal resolution of 6 hr,

179   published by Atlantic Oceanographic and Meteorological Laboratory, National Oceanic and

180   Atmospheric Administration (AOML/NOAA) (https://www.aoml.noaa.gov/hrd/data_sub/

181   wind.html) (Powell et al., 1998) and the North American Mesoscale (NAM) data, with a

182   spatial resolution of 12 km and a temporal resolution of 3 hr, provided by National Centers

183   for Environmental Prediction (NCEP) (https://www.ncdc.noaa.gov/data-access/model-

184   data/model-datasets/north-american-mesoscale-forecast-system-nam) (Janjic et al., 2004).

185   In our computation, the former is used between 26 and 31 August (during the hurricane

186   event) because it has a better accuracy in capturing the maximum wind speed, while the

187   latter is used during other periods of the simulation. Reanalysis data for other atmospheric

188   forcing, such as the surface air temperature, air pressure, relative humidity, radiation and

189   precipitation are also available from NAM for determining the surface buoyancy fluxes.

190   In this study, the boundary layer effect on the near inertial current is not directly

considered. The driving effect of the airflow on the near inertial current is reflected by adding a wind drag on the ocean surface. The wind drag τ_s, which is measure of the vertical flux of horizontal momentum, can be estimated through (Fairall et al., 1996):

$$\tau_s = \rho_a C_d u_{10}^{2} \tag{8}$$

where, ρ_a is the density of the air; C_d is the drag coefficient; u_{10} is the horizontal wind speed at the 10-m level. Traditionally, the drag coefficient C_d is expressed as a linear function of the wind speed. In this study, we adopt a more advanced formula that fits the numerical results obtained with an improved wave boundary layer model under extreme wind conditions (Chen and Yu, 2016; Chen et al., 2018; Xu and Yu, 2021):

$$C_d = C_{dw} + \frac{C_{d0} - C_{dw}}{(W_0 - W)^2}(u_{10} - W)^2 \tag{9}$$

where C_{d0} is a threshold value set to 0.001 for the wind stress at $u_{10} \leq W_0 = 5$ m/s, C_{dw} is the saturated wind stress coefficient and W is the saturation wind speed. We have

$$C_{dw} = \begin{cases} -1.86 \times 10^{-4} \ln \dfrac{gD}{W_D} + 0.0025 & \dfrac{gD}{W_D} \leq 3 \\ 0.00225 & \dfrac{gD}{W_D} > 3 \end{cases} \tag{10}$$

$$W = \begin{cases} 4.64 \ln(\dfrac{gD}{W_D}) + 42.6 & \dfrac{gD}{W_D} \leq 0.6 \\ W_D & \dfrac{gD}{W_D} > 0.6 \end{cases} \tag{11}$$

where W_D set to 40 m/s is the saturation wind speed in deep water. Except for the momentum flux, other air-sea fluxes, e.g., the sensible heat flux and the latent heat flux, are determined based on the conventional bulk parameterization scheme (see Fairall et al. (1996) for detailed description). The sea surface boundary condition is then required to satisfy:

$$\nu \frac{\partial \mathbf{u}}{\partial z} = \boldsymbol{\tau}_s \tag{12}$$

2.3 Observational data

During the passage of Hurricane Irene (2011), a network of High-frequency (HF)

radars measured the surface currents and a Slocum glider launched near New Jersey measured the vertical profiles of the temperature and the salinity (Roarty et al., 2010; Schofield et al., 2010). The measured data are used to verify the computational results in this study. In fact, they have been widely used in previous studies (Glenn et al., 2016; Seroka et al., 2016; Seroka et al., 2017).

HF Radars in the Mid-Atlantic Regional Association's Coastal Ocean Observing System are able to observe the surface currents. The recorded data have a temporal resolution of 1 hr and a spatial resolution of 6 km, and are assumed to be measured at an effective depth of around 2.7 m below the ocean surface based on Roarty et al. (2020). The data cover the MAB area from the coast to the shelf break. HF Radar measures the radial component of ocean surface currents based on the Doppler effect. The surface currents are determined by combining overlapping radials from different radars in the observational network using an optimal interpolation method (Roarty et al., 2010; Zhang et al., 2018). 'Coverage' is defined to represent how many overlapping radials are combined, and is thus closely related to the accuracy of data at a given point. Previous studies pointed out that the data are rather reliable when the 'coverage' is larger than 90% (Roarty et al., 2010; Kohut et al. 2012). Intrinsic HF Radar uncertainty has been estimated to be in the order of 5 cm/s (Brunner and Lwiza, 2020), indicating a relatively error of around 0.10 in regards to the surface current velocities. When compared with ADCP, the RMS difference of HF Radar is only within 8 cm/s (Roarty et al., 2010; Kohut et al. 2012; Roarty et al. 2020). In this study, HF Radar data are directly obtained from https://maracoos.org/ and spatially interpolated to the locations of our interest. All the data within the shelf break are found to be quite reliable since the 'coverage' there is larger than 90%. Note that the data outside the shelf break has a low coverage of 60%-90%. Though we use all the data as they are, we must remind that the data outside the shelf break should be viewed with caution.

Glider RU16 was an autonomous underwater vehicle of the Rutgers Slocum glider (Schofield et al., 2007, 2010) platform developed by Teledyne-Webb Research, and has demonstrated to be advantageous in marine monitoring, particularly under extreme weather

conditions (Glenn et al., 2016; Miles et al., 2017; Zhang et al., 2018). It was equipped with the Seabird un-pumped conductivity, temperature, and depth (CTD) sensor, and could thus measure not only the vertical profiles of the seawater temperature and the salinity but also the water depth. It was programmed to move vertically through the water column, collect data every 2 s, and surface at a 3 h interval to provide high temporal resolution data (Schofield et al., 2007; Glenn et al., 2016; Seroka et al., 2016). The RU16 dataset has been widely used and well verified by previous authors (Glenn et al., 2016; Seroka et al., 2016; Seroka et al., 2017). Therefore, it is used as it is in this study. The dataset is available at https://tds.marine.rutgers.edu/thredds/dodsC/cool/glider.

3 Ocean Responses to Hurricane Irene

3.1 Effect of hurricane on ocean surface flow

As shown in Figure 1, Hurricane Irene (2011) entered the Mid-Atlantic Bight (MAB) area of the present interest at Cape Lookout, North Carolina as a Category-1 event at 12:00, 27 August, 2011 (UTC time, the same below) with a maximum sustained wind (MSW) of over 38 m/s. It continued to move northeastward and made a landfall at Atlantic City, New Jersey at 9:35, 28 August with a MSW of around 30 m/s. During its motion in the MAB area of our interest, the radius of the hurricane wind field (the area with wind speed $\geq$32.9 m/s) reached a large value of 140 km (Avila and Cangialosi, 2011).
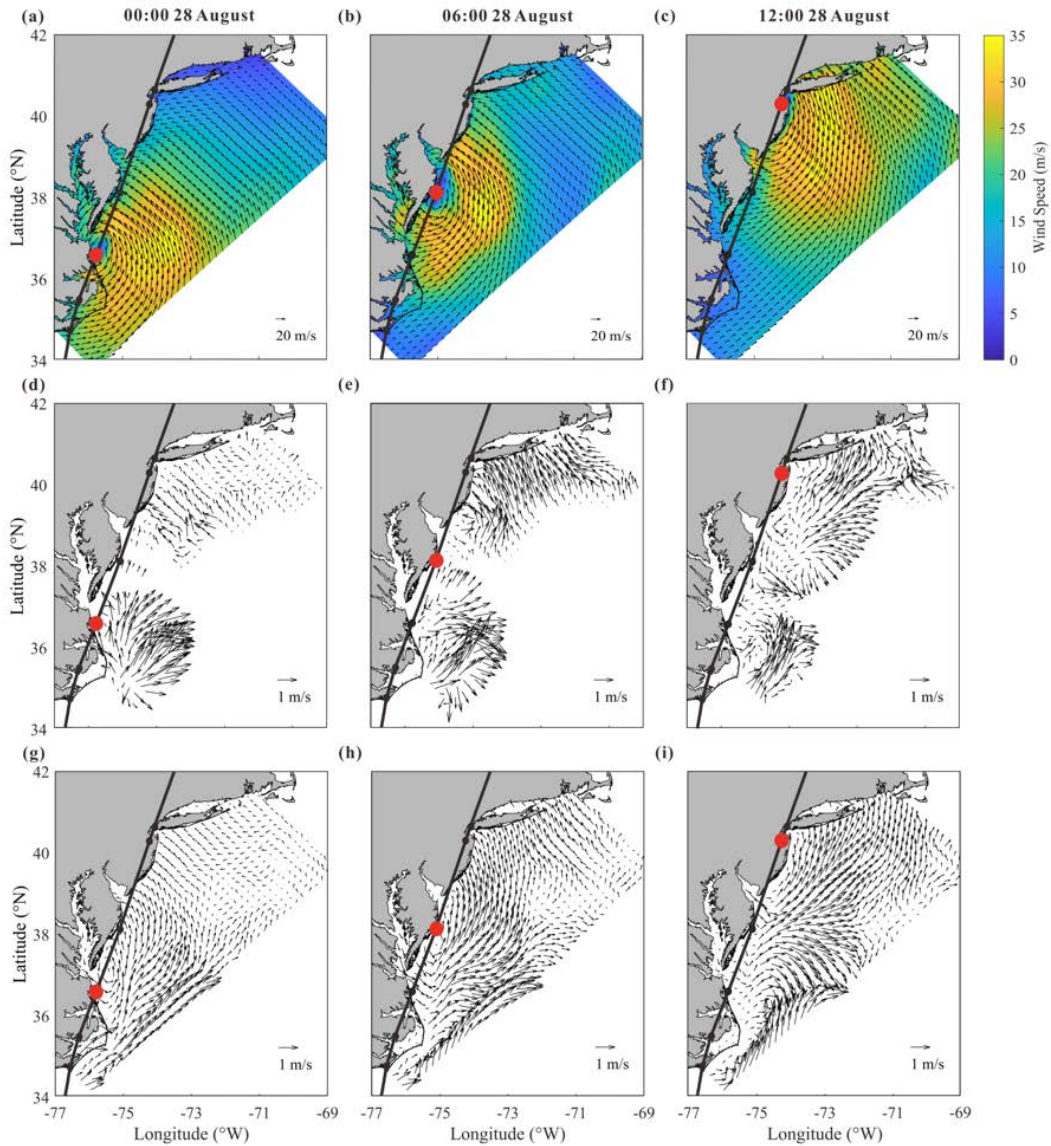
Figure 2. Snapshots of (a-c) the 10-m wind provided by H*WIND, (d-f) computed current velocity of the surface layer and (g-i) observed current velocity of the surface layer, at (left column) 00:00, (middle column) 06:00 and (right column) 12:00, 28 August, during the passage of Hurricane Irene (2011). Note that best track of the hurricane reported by Avila and Cangialosi (2011) is shown by black lines while the hurricane center is shown by red circles.

Figure 2 provides the snapshots of the wind, the computed and observed currents in the MAB area at 00:00, 06:00 and 12:00, 28 August, 2011, respectively. Note that 00:00 and 12:00 correspond to the time when Hurricane Irene entered and left the area of our interest, respectively. The wind field is plotted from the H*WIND data, while the field currents are obtained by the HF Radars and detided with Matlab toolbox T_TIDE (Pawlowicz et al.,

271   2002).

272   The computed current velocity of the surface layer, as shown in Figure 2d-f, is

273   compared with the observed one, as shown in Figure 2g-i, to verify the reliability of the

274   numerical model presented in this study. At 00:00, 28 August, it is numerically demonstrated

275   that currents rotating counterclockwise with a magnitude of over 1 m/s are rapidly generated

276   by the wind near the hurricane center (Figure 2d). In the observed results, though there are

277   significant data missing near the hurricane center, northeastward currents can still be

278   identified on the offshore waters along North Carolina coast (Figure 2g) and are in

279   reasonable agreement with the computed current field. Moreover, both computational and

280   observational results support a fact that the onshore wind (Figure 2a) on the front side of the

281   hurricane drives an onshore current with magnitude of 0.4 m/s along the northern MAB,

282   especially in the nearshore area of New Jersey (Figure 2d and 2g). At 06:00, Hurricane Irene

283   arrived at the offshore waters of Delmarva Peninsula. In spite of the field data missing, the

284   rotating currents induced by the hurricane wind can be clearly recognized in both computed

285   and observed results in the nearshore area of New Jersey (Figure 2e and 2h). In addition,

286   relatively strong onshore currents with magnitude of over 1 m/s are observed near Long

287   Island and are also well represented in the numerical results (Figure 2e). At 12:00, i.e., the

288   time when the hurricane left the area of our interest, the counterclockwise rotating currents

289   are still formed near the hurricane center as demonstrated by both computational and

290   observational results (Figure 2f and 2i). At the same time, clockwise rotating currents are

291   shown to be generated near Delmarva Peninsula in southern MAB after the hurricane passed

292   over. This fact is certainly confirmed by both computed and observed results, indicating

293   near inertial currents are activated after the hurricane event. Therefore, it becomes evident

294   that the rotating wind of the hurricane immediately forces a rotating current in the surface

295   layer of the ocean and induces an inertial current rotating in the opposite direction shortly

296   after the hurricane passed over. It is also worthwhile to emphasize that, in general, the

297   numerical results obtained with the present model agree fairly well with observed data.

3.2 Effect of hurricane on vertical stratification and sea surface cooling

Shown in Figure 3a is the vertical profile of the seawater temperature measured by Glider RU16 launched off the New Jersey Coast. It provides a good chance for us to validate the response of stratification to the hurricane event, which is likely one of the most important results of hurricane-ocean interaction. In Figure 3a, it is seen that the mixed layer off New Jersey coast was quite thin, with a thickness of less than 10 m, before the hurricane event. A strong stratification was clearly formed over a water depth of 40 m, with a surface temperature of 24 °C and a bottom temperature of 10 °C. When the hurricane center passed over the position of Glider RU16 at around 09:30, 28 August, the thickness of the mixed layer rapidly increased to nearly 30 m while the surface temperature was decreased by more than 5 °C, indicating a strong mixing process has occurred. By plotting the time series of the squared buoyancy frequency N based on the measured data, expansion of the mixed layer due to the hurricane event may be more vividly demonstrated (Figure 3c).
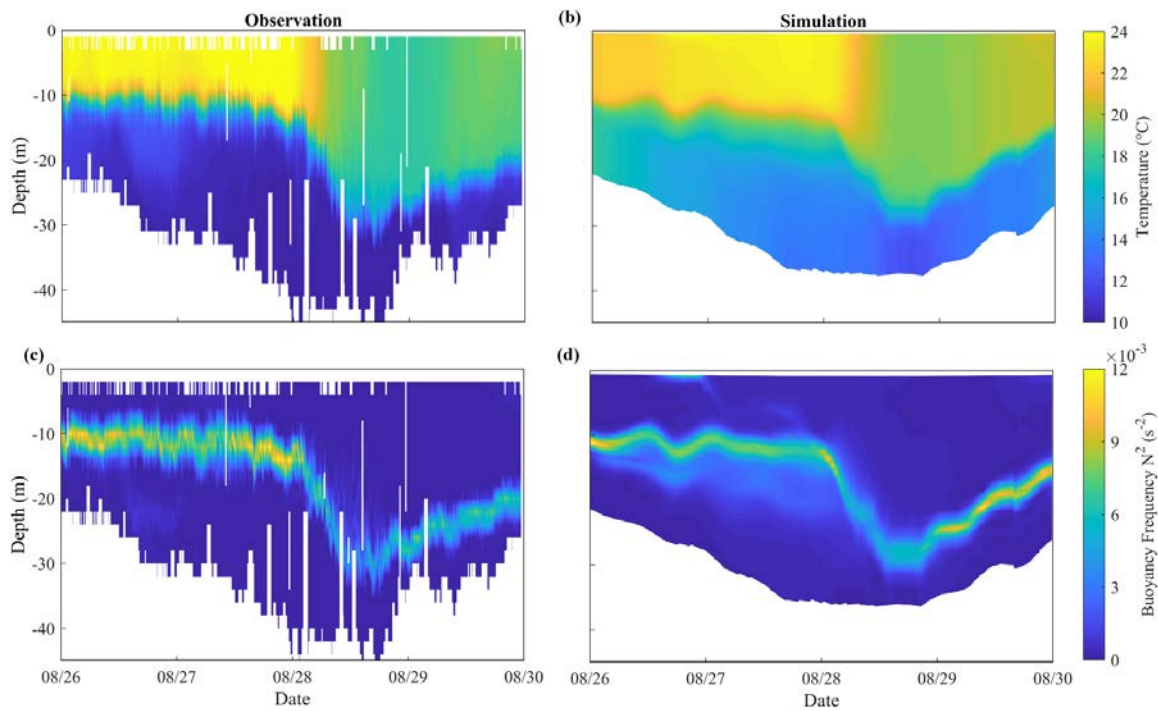

Figure 3. Time series of the vertical profiles of (top row) the temperature and (bottom row) the squared buoyancy frequency, obtained from (a, c) Glider RU16 and (b, d) numerical model.

317   Figure 3b and 3d present the computed results for the vertical distribution of seawater

318   temperature obtained by virtually setting a measuring point moving with the glider in the

319   real situation. The numerical results show a similar variation of the stratification pattern as

320   observed before and during the hurricane event. They reproduce both extension of the mixed

321   layer and cooling of the sea surface, indicating that the numerical model is capable of

322   describing the development and destruction of ocean stratification. However, a sea surface

323   cooling of about 4 °C obtained by the numerical model is a little smaller than 6-7 °C

324   observed by the glider in the field, probably due to the inaccurate setting of the initial bottom

325   temperature in the computation. Discrepancies of the squared buoyancy frequency N was

326   also found in the thermocline (Figure 3c), where the temperature varied most dramatically.

327   They are probably caused by the inaccurate setting of the initial temperature profile. In fact,

328   the initial condition for the bottom temperature in HYCOM is somehow higher (about 4°C)

329   than the observed value in the field if Figures 3a and 3b are compared. To correct this system

330   error, the real-time profile obtained from RU16 is used for a nudging process in computation,

331   i.e., the model temperature and salinity fields are forced to nudge toward observed data (see

332   Thyng et al. (2021) for detailed description).

333   The sea surface temperatures (SST) before and after the hurricane event are further

334   compared in Figure 4 (obtained from The Advanced Very High Resolution

335   Radiometer (AVHRR), https://earth.esa.int/eogateway/catalog/avhrr-level-1b-local-area-

336   coverage-imagery). Before the hurricane event, both observed and computed SST show

337   similar patterns, i.e., the SST decreases with the increasing latitude. After the hurricane

338   passage, the strong mixing and cooling mainly take place in shallow waters, where the initial

339   stratification is strong (Zhang et al., 2016), especially near New Jersey and Long Island.

340   However, the cooling is not prominent in shallow waters near North Carolina. In fact, it has

341   been reported that the SST in this region had decreased and then recovered to its pre-

342   hurricane level within only 1 day (Seroka et al., 2016). In fact, the HYCOM data showed

343   that the initial bottom temperature near North Carolina was as high as 18 °C. Considering

344   that sea surface cooling was positively related to the vertical temperature gradient (Shay and

Brewster, 2010; Vincent et al., 2012; Zhang et al., 2016), the small amount of cold pool

water in this region may have caused insignificant cooling and fast recovering.
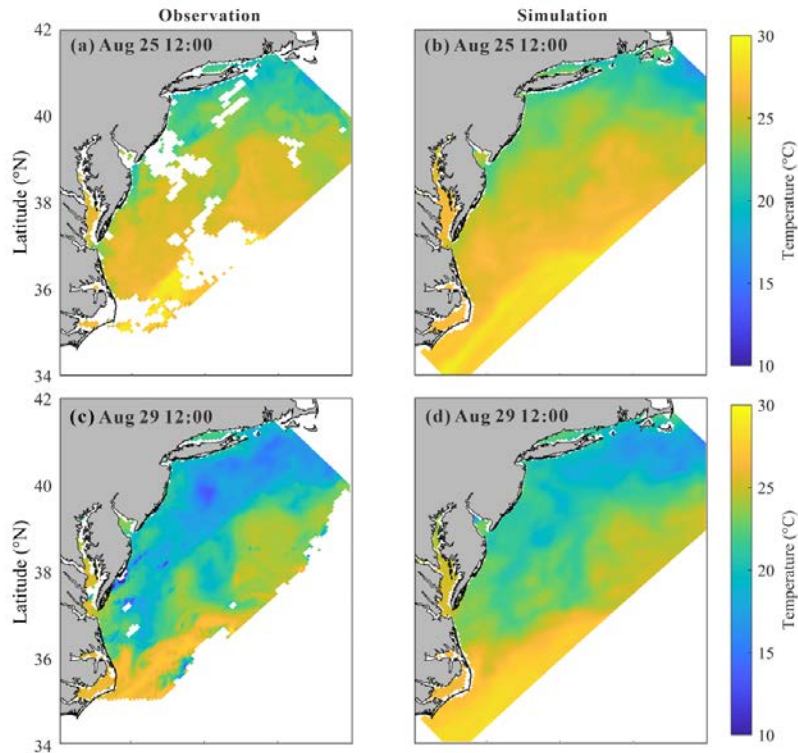
Figure 4. Sea surface temperature at Aug 25 12:00, before the hurricane event (top row) and at Aug 29 12:00, after the hurricane event (bottom row) from (a, c) observed data and (b, d) numerical model.

It should be pointed out that the computed SST cooling is 3-4 °C smaller than the observed one, which could also be explained by the inaccurate initial condition obtained from HYCOM. The HYCOM bottom temperature is somehow higher than actual, which could lead to the underestimation of the SST cooling. Therefore, we use the real-time SST data obtained from AVHRR for nudging process in computation to correct this system error (Thyng et al., 2021), considering that the accuracy of the initial stratification could obviously affect the modeling of mixing process. Note that the error is mainly caused by the discrepancy in initial settings but not the defects in numerical method. Thus this error could be calibrated in certain extent and thus would not affect the reliability of subsequent analysis, e.g. energy budget analysis.

3.3 Characteristics of NIC

To have a general understanding of the NICs in the MAB area induced by Hurricane Irene (2011), a network of 30 stations aligned on 5 cross-shore sections from south to north is introduced in this study to cover the area of our interest as shown in Figure 5, similar to Zhang et al (2018). In each section, 6 stations are placed in the cross-shore direction from the shore side to the deep ocean, where water depths are around 30 m, 50 m, 75 m, 120 m, and 220 m and 1000 m, respectively. Note that the most offshore stations are located outside the shelf break.
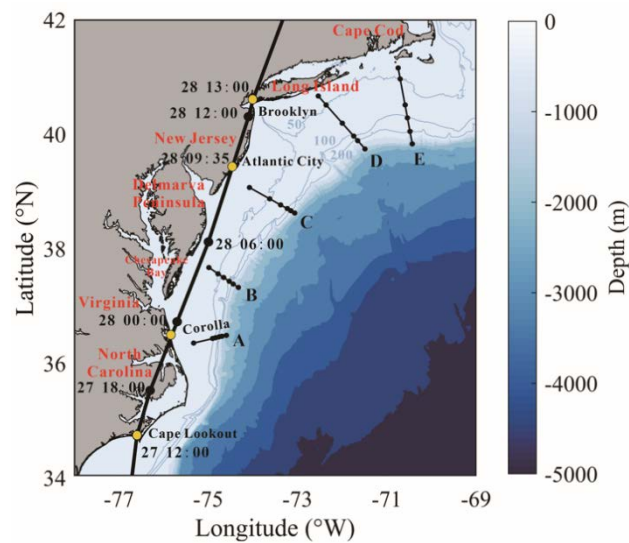

Figure 5. Five virtual sections marked by short black lines.

The velocity of NIC is obtained from the total current velocity by first excluding the tidal components and then passing it through a Butterworth filter with the frequency band of 0.8-1.2 f_0, an effective approach proposed by Hormann et al. (2014), Zhang et al. (2018) and Kawaguchi et al. (2020). Shown in Figure 6 are the time series of surface velocity of the NIC component in the cross-shore direction interpolated to 30 stations during the time period of our study (16 days from 20 August to 5 September). Results obtained with the numerical model are also presented. The alongshore component is similar to cross-shore component and thus omitted here. Intuitively, the numerical results are in reasonably good agreement with the HF Radar data. For a further discussion we define the near inertial kinetic energy (NIKE) in the following way:

17

$$E' = \frac{1}{2}\rho_0 \left|\mathbf{u}'\right|^2 \tag{13}$$

where, ρ_0 is the velocity of the NIC; $\mathbf{u}'$ is the seawater density at the standard atmospheric pressure. A phased corrected relative mean square error may then be introduced to describe the difference between the computed and observed NIKE:

$$\Delta = \frac{\min\limits_{\tau} \int_{t_0}^{t_1} \left[E'_O(t) - E'_C(t-\tau)\right]^2 dt}{\sqrt{\int_{t_0}^{t_1} \left[E'_O(t)\right]^2 dt}\sqrt{\int_{t_0}^{t_1} \left[E'_C(t)\right]^2 dt}} \tag{14}$$

where $E'_O(t)$ and $E'_C(t)$ are the observed and computed NIKE time series, respectively; $[t_0, t_1]$ is the duration when the hurricane-induced NICs are prominent, which is taken to be from August 25 to September 4 in this study; τ is a time shift for eliminating the phase error. We calculate Δ at all 30 stations. It is shown that Δ varies from 0.14-0.23 in most stations where the coverage is larger than 90%. However, it is also necessary to mention that in several nearshore stations, i.e. A1, D1 and E1, Δ exceeds 0.3, because the NIC is too weak at these stations as compared to the background currents. At the 6 stations outside the shelf break, i.e., at A6, C6 and D6, Δ even exceeds 0.5-0.6, implying that the HF Radar data is less accurate outside the shelf with low 'coverage'. As we mentioned in Section 2.3, the relative RMS difference of HF Radar data is around 0.10. Taking this intrinsic HF Radar uncertainty into consideration, $\Delta = 0.14$-0.23 in our study is quite acceptable. Therefore, we could conclude that our numerical results are in reasonably good agreement with the HF Radar data. Inaccuracy in the numerical results of the NICs may come from the minor errors in the wind forcing data because they are very sensitively related, e.g., underestimation at C3-C6 before the hurricane event may come from the errors in low-resolution NAM data used in pre-hurricane periods. In addition, error in the initial wind data may cause insignificant phase discrepancies in B3-B6.
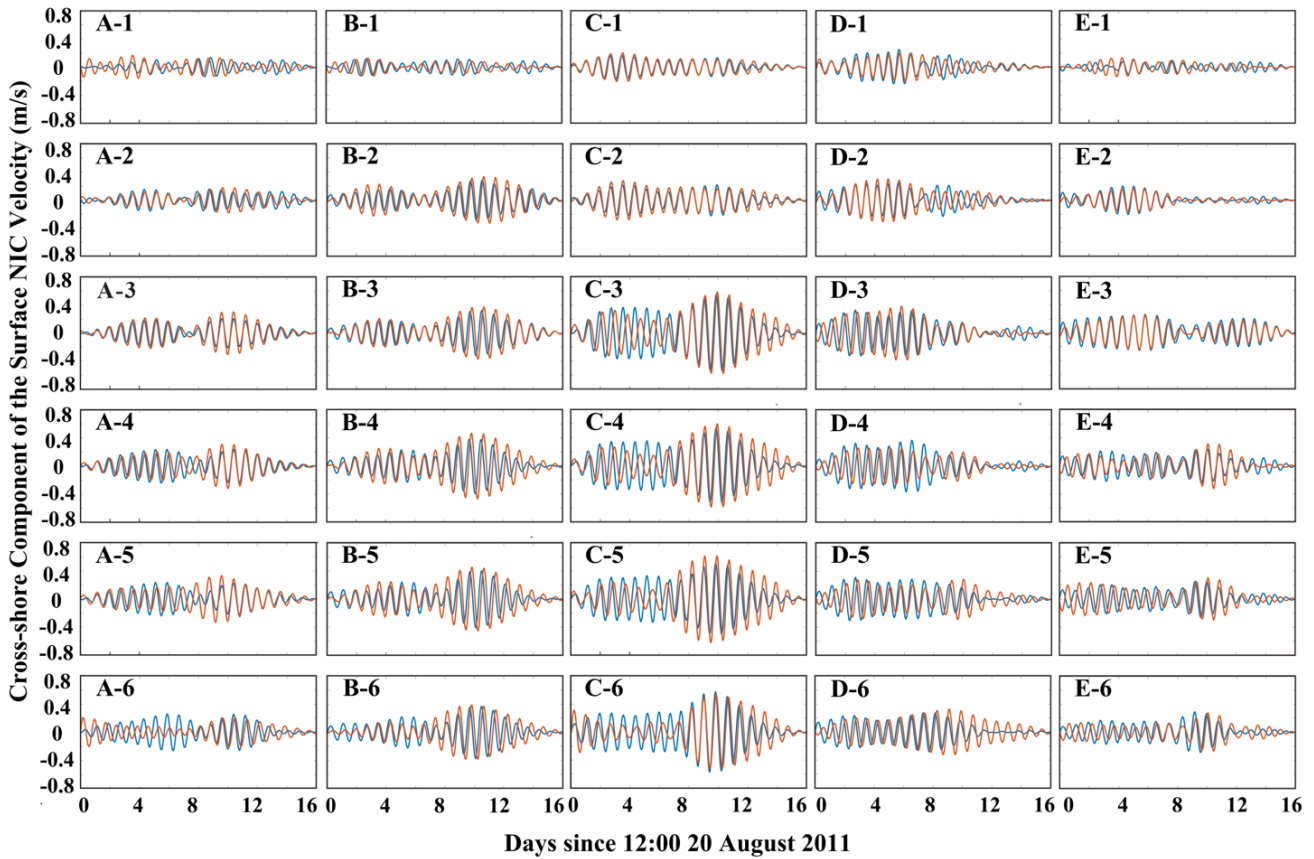
Figure 6. Time series of the NIC velocity in the surface layer obtained (blue line) by the HF Radar and (orange line) with numerical model at 30 stations along sections A-E.

In Figure 6, it can be readily recognized that, in the cross-shore direction from shallow to deep waters (i.e., Station No.1-No.5 in present study), the NIC velocity gradually increases by a factor of at least three, e.g., from 0.15 m/s to 0.6 m/s in section C, which is consistent with conclusions in previous studies (Kim and Kosro, 2013; Yang et al., 2015; Rayson et al., 2015; Zhang et al., 2018). This is because that NIC velocity in the nearshore region are restricted due to a combination of several reasons presented by Chen and Xie (1997), Rayson et al. (2015) and Chen et al. (2017). Different from other studies, however, the NIC velocity in the deep waters (i.e., Station No. 6 in the present study) is found to be not larger or even smaller than that nearby the shelf break. This is probably due to that fact that the track of Hurricane Irene (2011) was nearly attached to the shore during its motion in the area of our interest and the wind stress over the deep ocean was relatively small. From south to north, it is found that the NIC velocity in the middle regions, such as along section

19

422   C, is larger than those in south and north. By checking the numerical results, it is found that

423   the stratification was only slightly destroyed during the hurricane event near section C as

424   compared to the adjacent sections, which thus provided a better environment for NIC

425   generation (Yang et al., 2015; Shen et al., 2017).

426   To evaluate the relative importance of the near inertial currents, the rotary spectra of

427   the surface current velocity during the period of study (16 days) at different stations are

428   shown in Figure 7. The tidal flows corresponding to the major constituents M2, N2 and K1,

429   obtained with ADCIRC, are also plotted. It is seen that the velocity of the NICs is of an

430   equivalent magnitude to that of the M2 tidal current at the shallow-water stations where the

431   water depth is about 30 m (section C was taken for an example, Figure 7a). But, the velocity

432   of the NICs is significantly larger than that of the tidal current in deeper regions (Figure 7b,

433   c). It may be necessary to point out that weak NICs are not limited to the most nearshore

434   stations. In section D, for example, it is extended to a water depth of 75 m (Station D3,

435   Figure 7d) due to the severe destruction of stratification. However, the stratification outside

436   D3 was relatively well maintained due to the thicker mixed layer in these regions and the

437   farther distance from the main hurricane track. As discussed in the previous subsection, the

438   weak NICs in the nearshore area are closely related to the destruction of stratification by the

439   strong mixing process associated to the hurricane event (Yang et al., 2015; Shen et al., 2017).

440   However, this effect does not challenge the dominant role of NICs in deep waters.
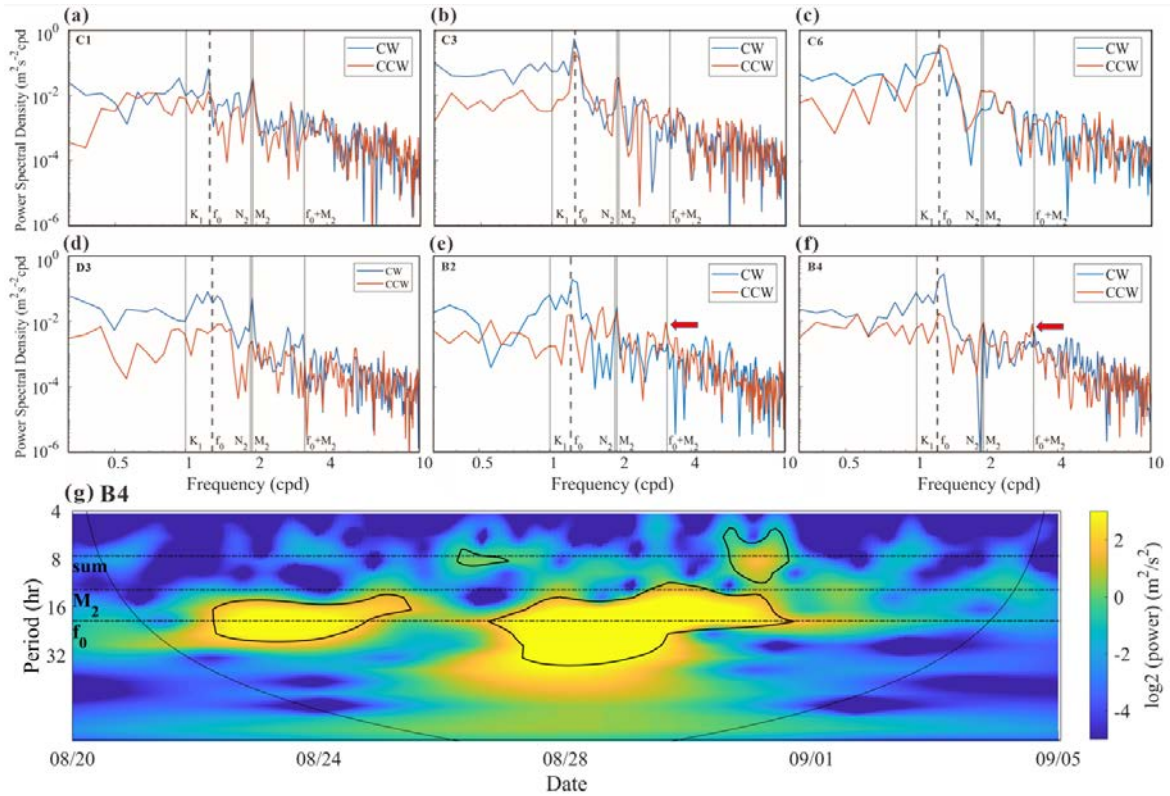
Figure 7. The rotary spectra of the current velocity in the surface layer during the simulation time (16 days) obtained by HF Radar at Stations (a) C1 (~30m), (b) C3 (~75m), (c) C6 (~1000 m), (d) D3, (e) B2 and (f) B4. Clockwise and counter-clockwise components of the current are shown by blue and orange lines, respectively (NICs are considered to be dominated by the clockwise component). The frequencies of the major tidal constituents M2, N2 and K1, the inertial frequency f0, and the sum-frequency of M2 and f_0 are all marked by gray lines. (g) Wavelet power spectrum for 10-30 m depth-averaged alongshore current component at Station B4 (see Thiebaut and Vennell (2010) for detailed description). Black contours indicate the 5% significance level against red noise and the arc line indicate the cone of influence.

Previous studies reported the nonlinear wave-wave interaction could transfer energy from the M2 tide and NIC into a wave at the sum of their frequencies (fM2). The key mechanism is the coupling between the vertical shear in NIC and the vertical velocity due to the internal tide (Davis and Xing, 2003; Hopkins et al., 2014; Shen et al., 2017; Wu et al., 2020). Though the M2 tide is rather strong in shallow waters during the hurricane event (Figure 7), nonlinear wave-wave interaction between the tidal current and the NIC could be hardly identified in most part of MAB. Nevertheless, a peak of the energy spectrum seems

21

460 to appear at the sum-frequency fM2 for the surface velocity at Stations B1 to B4, near

461 Delmarva Peninsula (B2 and B4 were taken as examples in Figure 7e, f). The evolution of

462 energy power at different frequencies for the middle-layer averaged (i.e., 10-30 m) currents,

463 where the flow shear is concentrated, is further demonstrated based on wavelet analysis

464 (Station B4 was taken as an example in Figure 7g). A peak energy at the sum-frequency fM2

465 is clearly identified after the hurricane passage. In fact, the subsequent Section 4.2 in this

466 paper will show that the strongest shear is found in offshore waters between Delmarva

467 Peninsula and New Jersey, i.e., near sections B and C (Figure 9a). Besides, Brunner and

468 Lwiza (2020) indicated that the most prominent M2 tide in southern MAB is located off

469 Delmarva Peninsula (near section B), according to a long-term observed data. Therefore,

470 the vertical shear in NIC and the vertical velocity due to the M2 tide is more likely to be

471 coupled in this region (i.e., near section B). However, this interaction only occurs in limited

472 regions and thus would not influence the NIC evolution in most part of MAB.

4 Near Inertial Kinetic Energy

4.1 Conservation of NIKE

475   For description of the intensity of a NIC, the near inertial kinetic energy (NIKE) may

476 be defined in Eq. (13). Note that the NIKE is mainly gained from the wind power and

477 dissipated due to a few mechanisms. Evolution of the vertically integrated NIKE within a

478 water column from the sea bottom the ocean surface is thus governed by (Zhai et al., 2009)

$$\int_{-d}^{\eta} \frac{\partial E'}{\partial t} dz = \boldsymbol{\tau}_s \cdot \mathbf{u}'_s + \boldsymbol{\tau}_b \cdot \mathbf{u}'_b - \int_{-d}^{\eta} \rho_0 \nu_e \left| \frac{\partial \mathbf{u}'}{\partial z} \right|^2 dz -$$

$$\int_{-d}^{\eta} \nabla \cdot \left(\mathbf{u}' p' \right) dz - \int_{-d}^{\eta} \rho' g w' dz - \int_{-d}^{\eta} \nabla \cdot \left(\mathbf{U} E' \right) dz + \text{others}$$

(15)

480 where, $\mathbf{u}'_s$ and $\mathbf{u}'_b$ are near inertial velocities at sea surface and bottom, respectively; $\mathbf{U}$

481 is the sub-inertial velocity; ρ' is the perturbation density, defined by $\rho' = \rho - \rho_*$; ρ_* is

482 the reference density, i.e., the density corresponding to a flattened stratification where the

483 fluid is redistributed adiabatically to a stable and vertically uniform state from the actual

484 condition (Holliday and McIntyre, 1981; Kang and Fringer, 2010; MacCready and Giddings,

485   2016); p' is the perturbation pressure, defined by $p' = g\int_{z}^{\eta}\rho'dz$. Terms on the right-hand

486   side of Eq. (13) are the wind energy input, the dissipation due to bottom friction, the vertical

487   diffusion due to turbulence, the horizontal divergence of near inertial energy flux, the

488   conversion between kinetic and potential energy, and the advection of NIKE by the sub-

489   inertial flow. The last term 'others' includes nonlinear transfer of energy between NICs and

490   flows of other frequencies as well as the horizontal diffusion due to mixing. Note that the

491   energy are integrated over the water column from $z = -d$ to free surface $z = \eta$. In

492   shallow waters, d is the actual water depth, while in deep waters, d is truncated to 200

493   m (i.e., the depth of the shelf break). When the bottom boundary is set at $z = -200\ \mathrm{m}$, the

494   bottom friction vanishes in Eq. (13) but a term related to the downward energy flux, i.e.,

495    $p'w'\big|_{z=-200m}$ should be added.

496   For a general understanding, distribution of the depth-integrated NIKE averaged over

497   a 10-day period from August 25 to September 4 is presented in Figure 8a. The wind power

498   integrated over the same period is plotted in Figure 8b. It is clearly shown in Figure 8a that

499   the high NIKE region mainly located in the offshore waters of Delmarva Peninsula and New

500   Jersey rather than in the nearshore area. This distribution pattern is rather similar to that of

501   the wind energy input, as presented in Figure 8b, indicating that the NIKE was immediately

502   gained from the wind power (Rayson et al. 2015; Shen et al., 2017; Zhang et al., 2018). In

503   fact, the NIKE could also come from other processes apart from the wind energy input

504   (Alford et al, 2016), meanwhile the wind energy input may also be transferred to energy of

505   waves apart from NIC (Chen at el., 2017), which leads to differences between Figure 8a and

506   7b.
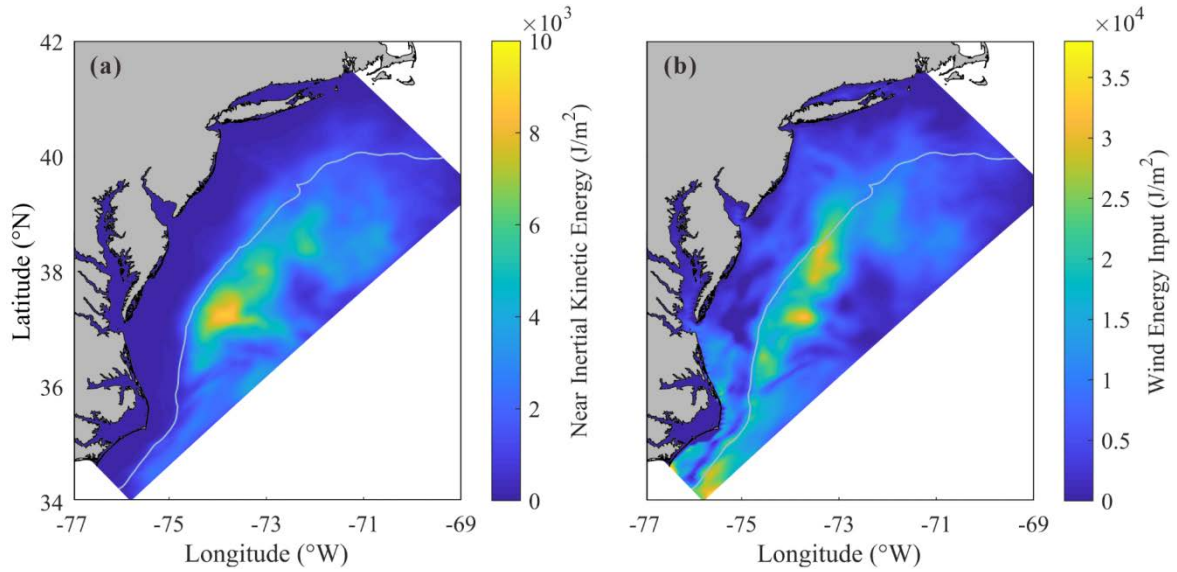
Figure 8. Spatial distribution of (a) depth-integrated near inertial kinetic energy averaged over the 10-day period and (b) wind power input to NICs integrated over the 10-day period.

Table 1. The contribution of each mechanism to energy budget. Percentages in parentheses refer to the ratio of each factor to wind energy input.

| Factor (J)	Contribution in Region A	Contribution in Region B
Wind Energy Input	7.75×10^{14}	3.16×10^{14}
Vertical Turbulence Diffusion	3.12×10^{14} (40%)	2.12×10^{14} (67%)
Lateral Divergence	1.34×10^{14} (17%)	5.69×10^{13} (18%)
Downward Transfer	2.58×10^{14} (33%)	0
Advection	3.33×10^{13} (4%)	1.04×10^{13} (3%)
Conversion	6.9×10^{12} (1%)	1.58×10^{13} (5%)
Bottom Friction	0	7.58×10^{13} (24%)

An important objective of the present study is to identify the mechanism of NIC development and decay. For this purpose, we consider a rectangular domain and separate it into deep water region A (depth > 200 m) and continental shelf region B (depth ⩽ 200 m), as depicted in Figure 1a. If the NICs are considered to be negligibly weak before and after

518   Hurricane Irene (2011), we may try to find how the wind power that drives the NICs during

519   the hurricane event is balanced, by comparing the accumulated contribution of different

520   mechanisms. Performing an integration of each terms in Eq. (13) with respect to time over

521   10 days from August 25 to September 4 and with respect to the horizontal coordinates over

522   both deep water region A and continental shelf region B, the contribution of each mechanism

523   to the energy budget is obtained as shown in Table 1. It is clearly demonstrated that in the

524   deep water region, the wind energy input was basically balanced by the vertical diffusion

525   due to turbulence (40%) and a downward transfer of the near inertial energy to the deep

526   ocean (33%). In the continental shelf region, the vertical diffusion due to turbulence

527   dominated the dissipation of NIKE (nearly 70%), while the bottom friction played a

528   secondary role (24%). It is worthwhile mentioning that lateral divergence of NIKE should

529   not be neglected in both shallow and deep water regions under the hurricane condition

530   (nearly 20%), different from previous studies which focused on NICs under the local wind

531   condition or in a broader research region across the whole North Atlantic (Chant, 2001; Zhai

532   et al., 2009; Shen et al., 2017). Other processes, e.g., advection due to sub-inertial flows,

533   only played a minor role. Note that the ratio of near inertial energy decay to wind energy

534   input exceeded 100% in the continental shelf region, confirming that NIKE may be gained

535   from other sources in addition to wind energy input in nearshore regions (Alford et al., 2016).

4.2 Decay of NIKE

537   The spatial distribution of the time-integrated energy dissipated through vertical

538   diffusion due to turbulence is plotted in Figure 9a. It is seen that a large amount of the

539   dissipation occurred at the offshore side of the continental shelf (i.e., at the offshore side of

540   the shallow region B), which does not coincide with the region where the wind energy input

541   is intense as demonstrated in Figure 8b. This implies that dissipation of NIKE is not mainly

542   caused by an increased intensity of turbulence, which certainly takes place in a region where

543   wind energy input achieves a high level (Zhai et al., 2009; Zhang et al., 2018). For a more

544   detailed discussion, the averaged eddy viscosity ν_e and the averaged vertical shear rate of

545   NIC $\left| \partial \mathbf{u}' / \partial z \right|^2$ during the period of our study are presented in Figure 9b and 8c. It is then

confirmed that the strong vertical shear also occurred at the outer half of the continental

shelf. The eddy viscosity, however, has a completely different distribution. In conclusion,

the vertical shear, known to be closely related to the ocean stratification (Shen et al., 2017),

plays a crucial role in the turbulence diffusion. It happened that one of the well-known

sharpest thermoclines in the world exists in the coastal water of MAB (Schofield et al., 2008;

Lentz, 2017). It may be necessary to emphasize that, although the stratification in the

shallowest water was totally destroyed during the hurricane event, as mentioned in Section

3, the seawater at the outer half of the continental shelf still partly maintained its

stratification.
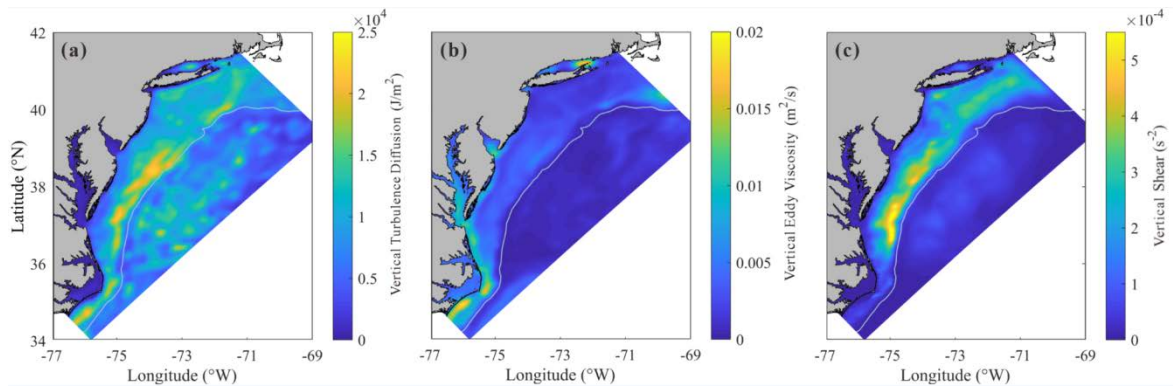
Figure 9. Spatial distribution of (a) depth-integrated vertical diffusion due to turbulence integrated over the 10-day period, (b) depth-averaged vertical eddy viscosity and (c) depth-averaged vertical shear, both averaged over the 10-day period.

The lateral divergence of NIKE flux, which also results in decay of NIKE and is not

trivial (~20%) in both shallow and deep water regions, may have to be discussed in some

details. As shown in Eq. (13), the lateral divergence of NIKE flux is a vertical integration

of $\nabla \cdot \left(\mathbf{u}' p' \right)$, which may also be expressed as an equivalent integration of $\nabla \cdot \left(\mathbf{c}' E' \right)$,

where $\mathbf{c}'$ is the transport velocity of NIKE in the horizontal plane (Price, 1994). When

compared to previous studies (Zhai et al., 2009), which dealt with the normal wind induced

NIC over a large part of the North Atlantic and showed that the lateral divergence accounted

only for less than 5% of the total NIKE loss, we focused only on the hurricane-affected

region. In the hurricane-affected region, the larger NIKE gradient naturally leads to a larger

divergence. If we extend the domain of study by a factor of 1.5, however, contribution of

the averaged lateral divergence decreases by more than half. It is thus strongly implied that

the lateral divergence of NIKE flux is significant within the hurricane-affected region.

It is also of interest to note that the contribution of the lateral divergence in south region

of our computational domain is less than 8%, much smaller than the average value of ~20%.

Several studies have pointed out that the transport velocity $\mathbf{c}'$ is largely influenced by the

background vorticity gradient (Zhai et al., 2009; Park et al., 2009). In other words, NIKE

can hardly be transferred from a place of lower background vorticity to a place of higher

background vorticity or, NIKE can hardly penetrate a vorticity ridge from either side. Shown

in Figure 10 is the distribution of the background vorticity within our computational domain

during the hurricane event (data from https://resources.marine.copernicus.eu/product-

detail/SEALEVEL_GLO_PHY_CLIMATE_L4_MY_008_057/INFORMATION).   A

remarkable vorticity ridge exists in the southeast of the computational domain, which is

considered to be caused by the strong horizontal shear at the edge of Gulf Stream (a warm

and swift ocean current in Atlantic, flowing through the southern MAB and propagating

northeastward). This vorticity ridge can reduce the lateral divergence of NIKE flux in south

region of our computational domain.
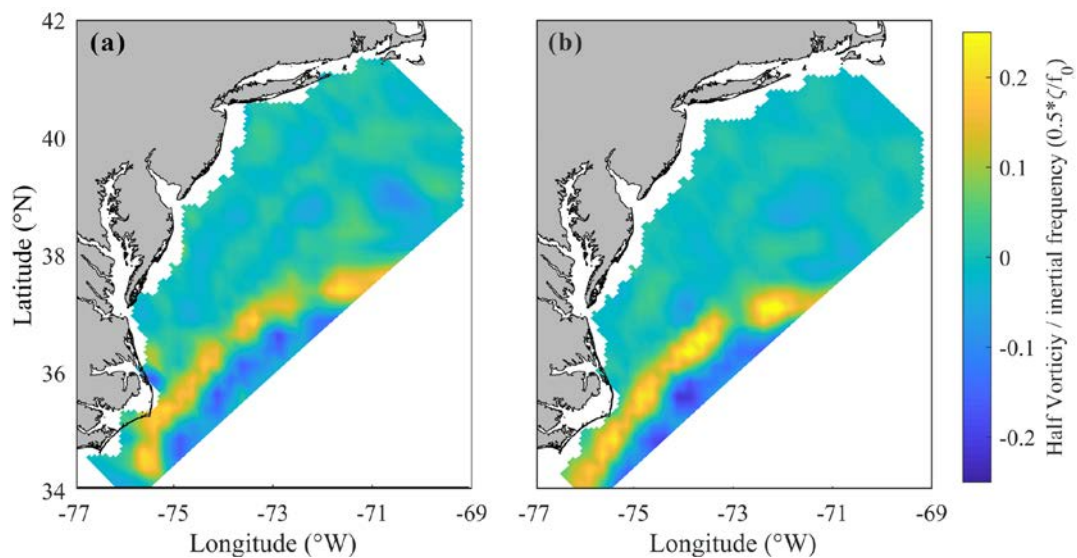
Figure 10. Spatial distribution of background vorticity (a) before the hurricane event on Aug
25 and (b) after the hurricane event on Sep 4.

4.3 Decay timescale of NIKE

It is of practical importance to determine the rate of NIKE decay. A conventional measure of the rate of NIKE may be its e-folding time, i.e., the timescale in which the NIKE decreases by a factor of e. Shown in Figure 11 is the e-folding time of the depth-integrated NIKE at 24 stations along sections A to D. The decay timescale in section E is not considered because this section is relatively far from the hurricane track as compared with other sections and also because the orientation of section E differs quite significantly from that of other sections.
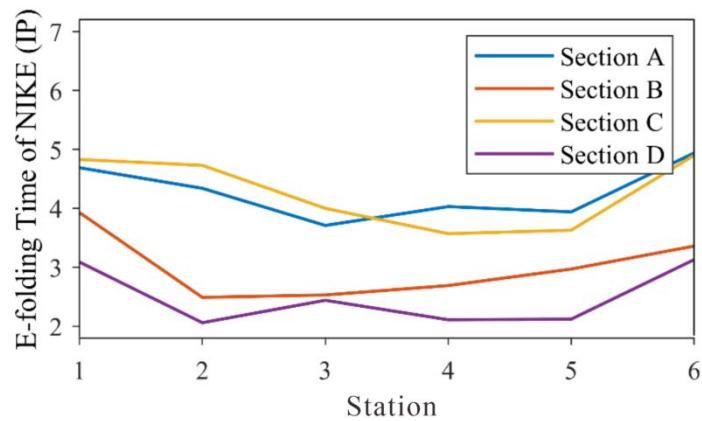
Figure 11. The decay timescale of the depth-integrated NIKE at 24 stations along sections A to D. Note that the unit for the e-folding time is the inertial period.

It is interesting to note that the decay timescales in the shallow and deep regions are fairly different. As shown in Figure 11, the NIKE is dissipated much more slowly outside the shelf break (Station No.6) than over the continental shelf. This difference is often considered to be an effect of the bottom friction and the extremely strong turbulence in the shallow waters, as pointed out by other researchers (Rayson et al., 2015; Shen et al., 2017). It is also interesting to find that the variation of NIKE decay rate in shallow waters is much more complicated than in the deep waters. In the cross-shore direction, the NIKE at the middle stations, i.e., Stations No. 3 to No. 5, located at the outer half of the continental shelf, is shown to be dissipated most rapidly, especially along sections A to C (Figure 11). This phenomenon is actually supported by the fact that the strongest turbulence diffusion

28

occurred over the outer half of the continental shelf, particularly in the relevant region between sections A and C (Figure 9a). Considering the variation of the wind energy input within the same section should not be too large, the ratio of turbulence diffusion to wind energy input must be mainly determined by the turbulence diffusion. Therefore, the strong turbulence dissipation due to the strong vertical shear in well-maintained stratification is responsible for the rapid energy decay in the outer half of the continental shelf, as shown in Section 4.2. Although the bottom friction also has some effect on the decay timescale of NIKE onshore, the turbulence effect is predominant.

In the alongshore direction, it is shown that the NIKE in sections B and D decayed more rapidly. Actually, the decay timescale there is only 2 to 3 inertial periods compared to 4 to 5 inertial periods in sections A and C. However, the limited variability of the turbulence diffusion in alongshore direction should not lead to such a big difference. Near section A, the vorticity ridge in Gulf Stream restricted the lateral divergence of NIKE, which may contribute to a long decay timescale to some extent. However, the role of this effect was limited. In fact, as mentioned in Section 3, the nonlinear wave-wave interaction near section B may have caused a transfer of NIKE to other frequencies, as also pointed out by Shen et al. (2017). In fact, it is found that the ratio of turbulence diffusion to wind input in section B was larger than in other sections by 20%-30%, due to the low level of wind input (Figure 8b) and high level of turbulence dissipation (Figure 9a) there. These factors combined seem to have yielded an extraordinarily short e-folding time in section B. In section D, due to the complete destruction of stratification after the hurricane event (as mentioned in Section 3 and shown in Figure 7d), the NICs were of the same order as the background flow (D1-D4 in Figure 6). Therefore, the decay timescale of NIKE in section D is certainly inaccurate and possibly meaningless.

5 Conclusion

This study is aimed to investigate the development and decay mechanism of NICs in the MAB area caused by Hurricane Irene (2011). Numerical results obtained with ROMS

are shown to agree well with the observational data. Both computational and observational results show that the rotating wind of the hurricane immediately forced a rotating current in the surface layer of the ocean and induced an inertial current rotating in the opposite direction about one inertial period after the hurricane passed over. The NICs overwhelmed M2 tide in most areas of the MAB region except in the nearshore area where the stratification was totally destroyed by the strong mixing due to turbulence. In addition, the cross-shore component of the NIC velocity gradually increases by a factor of at least three from a shallow-water position to the shelf break.

The energy budget in the NICs is investigated in both deep and shallow waters. NIKE was shown to be immediately gained from the wind power during the hurricane event. In the deep water region, NIKE was mainly dissipated by the vertical diffusion due to turbulence and partially transferred to deep waters. In the continental shelf region, NIKE was basically dissipated by the turbulence diffusion, meanwhile the bottom friction played a secondary role. The nonlinear wave-wave interaction only dissipated NIKE in limited regions, e.g. shelf waters off Delmarva Peninsula. Notably, the lateral divergence of NIKE should be taken into consideration in both shallow and deep water regions under the hurricane condition. However, in southern MAB, it was restricted by a vorticity ridge at the edge of Gulf Stream. It is also clarified that the NIKE dissipation due to turbulence diffusion is much more closely related to the rate of the vertical shear rather than the intensity of turbulence, which certainly takes place in a region where wind energy input achieves a high level. The strong vertical shear at the offshore side of the continental shelf leaded to the strong turbulence dissipation in this region.

Acknowledgements

Data Availability Statements

The data used in this study are listed below. In particular, the regional oceanic modeling system (ROMS) code is available at https://www.myroms.org; HF radar data is available at http://tds.marine.rutgers.edu/thredds/dodsC/cool/codar/totals/5Mhz_6km_realtime_fmrc/ Maracoos_5MHz_6km_Totals-FMRC_best.ncd.html; Glider data is available at http://tds.marine.rutgers.edu/thredds/dodsC/cool/glider/mab/Gridded/20110810T1330_epa _ru16_active.nc.html; HYCOM data is available at https://www.hycom.org/data/glbu0pt08/ expt-91pt2; ADCIRC data is available at https://adcirc.org/products/adcirc-tidal-databases; USGS data is available at https://waterdata.usgs.gov; H*WIND data is available at https://www.aoml.noaa.gov/hrd/data_sub/wind.html; NAM data is available at https://www.ncdc.noaa.gov/data-access/model-data/model-datasets/north-american-mesoscale-forecast-system-nam; C3S data is available at https://resources.marine.copernicus.eu/product-detail/SEALEVEL_GLO_PHY _CLIMATE_L4_MY_008_057/INFORMATION; AVHRR data is available at https://earth.esa.int/eogateway/catalog/avhrr-level-1b-local-area-coverage-imagery.

References

Alford, M.H., 2003a. Improved global maps and 54-year history of wind-work on ocean inertial motions. Geophysical Research Letters, 30(8).

Alford, M.H., 2003b. Redistribution of energy available for ocean mixing by long-range propagation of internal waves. Nature, 423(6936): 159-162.

Alford, M.H., MacKinnon, J.A., Simmons, H.L. and Nash, J.D., 2016. Near-inertial internal gravity waves in the ocean. Annual Review of Marine Science, 8(1): 95-123.

Allahdadi, M., 2014. Numerical experiments of hurricane impact on vertical mixing and de-stratification of the louisiana shelf waters. Ph. D. Thesis, Louisiana State University, Baton Rouge.

Amante, C. and Eakins, B.W., 2009. Etopo1 1 arc-minute global relief model: Procedures, data sources and analysis. NOAA Technical Memorandum NESDIS NGDC-24,

692   National Geophysical Data Center, NOAA.

693   Avila, L.A. and Cangialosia, J., 2011. Tropical cyclone report: Hurricane irene: August 21–

694   28, 2011. National Hurricane Center Report AL0920011, US National Oceaninc and

695   Atmospheric Administration's National Weather Service.

696   Brunner, K. and Lwiza, K.M.M., 2020. Tidal velocities on the mid-atlantic bight continental

697   shelf using high-frequency radar. Journal of Oceanography, 76(4): 289-306.

698   Castelao, R.M., 2014. Mesoscale eddies in the south atlantic bight and the gulf stream

699   recirculation region: Vertical structure. Journal of Geophysical Research: Oceans,

700   119(3): 2048-2065.

701   Chang, S.W. and Anthes, R.A., 1978. Numerical simulations of the ocean's nonlinear,

702   baroclinic response to translating hurricanes. Journal of Physical Oceanography,

703   8(3): 468-480.

704   Chant, R.J., 2001. Evolution of near-inertial waves during an upwelling event on the new

705   jersey inner shelf. Journal of Physical Oceanography, 31(3): 746-764.

706   Chassignet, E.P. et al., 2007. The hycom (hybrid coordinate ocean model) data assimilative

707   system. Journal of Marine Systems, 65(1): 60-83.

708   Chen, C., Reid, R.O. and Nowlin Jr, W.D., 1996. Near-inertial oscillations over the texas-

709   louisiana shelf. Journal of Geophysical Research: Oceans, 101(C2): 3509-3524.

710   Chen, C. and Xie, L., 1997. A numerical study of wind-induced, near-inertial oscillations

711   over the texas-louisiana shelf. Journal of Geophysical Research: Oceans, 102(C7):

712   15583-15593.

713   Chen, G., Xue, H., Wang, D. and Xie, Q., 2013. Observed near-inertial kinetic energy in the

714   northwestern south china sea. Journal of Geophysical Research: Oceans, 118(10):

715   4965-4977.

716   Chen, S., Chen, D. and Xing, J., 2017. A study on some basic features of inertial oscillations

717   and near-inertial internal waves. Ocean Science, 13(5): 829-836.

718   Chen, Y. and Yu, X., 2016. Enhancement of wind stress evaluation method under storm

719   conditions. Climate Dynamics, 47(12): 3833-3843.

720 Chen, Y., Zhang, F., Green, B.W. and Yu, X., 2018. Impacts of ocean cooling and reduced

721   wind drag on hurricane katrina (2005) based on numerical simulations. Monthly

722   Weather Review, 146(1).

723 Churchill, J.H., Wirick, C.D., Flagg, C.N. and Pietrafesa, L.J., 1994. Sediment resuspension

724   over the continental shelf east of the delmarva peninsula. Deep Sea Research Part II:

725   Topical Studies in Oceanography, 41(2): 341-363.

726 Cummings, J.A., 2005. Operational multivariate ocean data assimilation. Quarterly Journal

727   of the Royal Meteorological Society, 131(613): 3583-3604.

728 D'Asaro, E.A., 1985. The energy flux from the wind to near-inertial motions in the surface

729   mixed layer. Journal of Physical Oceanography, 15: 1043-1059.

730 Davies, A.M. and Xing, J., 2003. On the interaction between internal tides and wind-induced

731   near-inertial currents at the shelf edge. Journal of Geophysical Research: Oceans,

732   108(C3).

733 Derrick, T.R., Bates, B.T. and Dufek, J.S., 1994. Evaluation of time-series data sets using

734   the pearson product-moment correlation coefficient. Medicine and science in sports

735   and exercise, 26(7): 919-928.

736 Donelan, M.A. et al., 2004. On the limiting aerodynamic roughness of the ocean in very

737   strong winds. Geophysical Research Letters, 31(18).

738 Dorostkar, A., Boegman, L., Diamessis, P. and Pollard, A., 2010. Sensitivity of mitgcm to

739   different model parameters in application to cayuga lake. Proceedings of the 6th

740   International Symposium on Environmental Hydraulics, Two Volume Set, p.^pp.

741   373-378.

742 Emanuel, K.A., 1995. Sensitivity of tropical cyclones to surface exchange coefficients and

743   a revised steady-state model incorporating eye dynamics. Journal of the

744   Atmospheric Sciences, 52: 3969-3976.

745 Fairall, C.W., Bradley, E.F., Rogers, D.P., Edson, J.B. and Young, G.S., 1996. Bulk

746   parameterization of air-sea fluxes for tropical ocean-global atmosphere coupled-

747   ocean atmosphere response experiment. Journal of Geophysical Research: Oceans,

101(C2): 3747-3764.

Freeman, N.G., Hale, A.M. and Danard, M.B., 1972. A modified sigma equations' approach to the numerical modeling of great lakes hydrodynamics. Journal of Geophysical Research 77(6): 1050-1060.

Furuichi, N., Hibiya, T. and Niwa, Y., 2008. Model-predicted distribution of wind-induced internal wave energy in the world's oceans. Journal of Geophysical Research: Oceans, 113(C9).

Garrett, C., 2001. What is the "near-inertial" band and why is it different from the rest of the internal wave spectrum? Journal of Physical Oceanography, 31(4): 962-971.

Glenn, S.M. et al., 2016. Stratified coastal ocean interactions with tropical cyclones. Nature Communications, 7(1): 10887.

Gregg, M.C., 1987. Diapycnal mixing in the thermocline: A review. Journal of Geophysical Research: Oceans, 92(C5): 5249-5286.

Haidvogel, D.B. et al., 2008. Ocean forecasting in terrain-following coordinates: Formulation and skill assessment of the regional ocean modeling system. Journal of Computational Physics, 227(7): 3595-3624.

Hoarfrost, A. et al., 2019. Gulf stream ring water intrusion on the mid-atlantic bight continental shelf break affects microbially driven carbon cycling. 6.

Holliday, D. and McIntyre, M.E., 1981. On potential energy density in an incompressible, stratified fluid. Journal of Fluid Mechanics, 107: 221-225.

Hopkins, J.E., Stephenson Jr, G.R., Green, J.A.M., Inall, M.E. and Palmer, M.R., 2014. Storms modify baroclinic energy fluxes in a seasonally stratified shelf sea: Inertial-tidal interaction. Journal of Geophysical Research: Oceans, 119(10): 6863-6883.

Hormann, V., Centurioni, L.R., Rainville, L., Lee, C.M. and Braasch, L.J., 2014. Response of upper ocean currents to typhoon fanapi. Geophysical Research Letters, 41(11): 3995-4003.

Jackett, D.R. and McDougall, T.J., 1995. Minimal adjustment of hydrographic profiles to achieve static stability. Journal of Atmospheric and Oceanic Technology, 12(2): 381-

776   389.

777   Janjic, Z.I. et al., 2004, June. The ncep wrf core, 20th Conference on Weather Analysis and

778   Forecasting/16th Conference on Numerical Weather Prediction, Seattle, Washington,

779   pp. 10-25.

780   Jochum, M. et al., 2013. The impact of oceanic near-inertial waves on climate. Journal of

781   Climate, 26(9): 2833-2844.

782   Kang, D. and Fringer, O., 2010. On the calculation of available potential energy in internal

783   wave fields. Journal of Physical Oceanography, 40(11): 2539-2545.

784   Kawaguchi, Y., Wagawa, T. and Igeta, Y., 2020. Near-inertial internal waves and multiple-

785   inertial oscillations trapped by negative vorticity anomaly in the central sea of japan.

786   Progress in Oceanography, 181: 102240.

787   Kim, S.Y. and Kosro, P.M., 2013. Observations of near-inertial surface currents off oregon:

788   Decorrelation time and length scales. Journal of Geophysical Research: Oceans,

789   118(7): 3723-3736.

790   Kohut, J., Roarty, H., Randall-Goodwin, E., Glenn, S. and Lichtenwalner, C.S., 2012.

791   Evaluation of two algorithms for a network of coastal HF Radars in the Mid-Atlantic

792   Bight. Ocean Dynamics, 62(6): 953-968.

793   Kunze, E., 1985. Near-inertial wave propagation in geostrophic shear. Journal of Physical

794   Oceanography, 15(5): 544-565.

795   Lentz, S.J., 2017. Seasonal warming of the middle atlantic bight cold pool. Journal of

796   Geophysical Research: Oceans, 122(2): 941-954.

797   Li, M., Zhong, L., Boicourt, W.C., Zhang, S. and Zhang, D.-L., 2007. Hurricane-induced

798   destratification and restratification in a partially-mixed estuary. Journal of Marine

799   Research, 65(2): 169-192.

800   MacCready, P. and Giddings, S.N., 2016. The mechanical energy budget of a regional ocean

801   model. Journal of Physical Oceanography, 46(9): 2719-2733.

802   MacKinnon, J.A. and Gregg, M.C., 2005. Near-inertial waves on the new england shelf:

803   The role of evolving stratification, turbulent dissipation, and bottom drag. Journal

804   of Physical Oceanography, 35(12): 2408-2424.

805   Marchesiello, P., McWilliams, J.C. and Shchepetkin, A., 2001. Open boundary conditions

806   for long-term integration of regional oceanic models. Ocean Modelling, 3(1): 1-20.

807   Miles, T., Seroka, G. and Glenn, S., 2017. Coastal ocean circulation during hurricane sandy.

808   Journal of Geophysical Research: Oceans, 122(9): 7095-7114.

809   Mulligan, R.P. and Hanson, J.L., 2016. Alongshore momentum transfer to the nearshore

810   zone from energetic ocean waves generated by passing hurricanes. Journal of

811   Geophysical Research: Oceans, 121(6): 4178-4193.

812   Munk, W. and Wunsch, C., 1998. Abyssal recipes ii: Energetics of tidal and wind mixing.

813   Deep Sea Research Part I: Oceanographic Research Papers, 45(12): 1977-2010.

814   Olabarrieta, M., Warner, J.C. and Kumar, N., 2011. Wave-current interaction in willapa bay.

815   Journal of Geophysical Research: Oceans, 116(C12).

816   Park, J.J., Kim, K. and Schmitt, R.W., 2009. Global distribution of the decay timescale of

817   mixed layer inertial motions observed by satellite-tracked drifters. Journal of

818   Geophysical Research: Oceans, 114(C11).

819   Pawlowicz, R., Beardsley, B. and Lentz, S., 2002. Classical tidal harmonic analysis

820   including error estimates in MATLAB using T_TIDE. Computers & Geosciences,

821   28(8): 929-937.

822   Pollard, R.T., 1980. Properties of near-surface inertial oscillations. Journal of Physical

823   Oceanography, 10(3): 385-398.

824   Powell, M.D., Houston, S.H., Amat, L.R. and Morisseau-Leroy, N., 1998. The hrd real-time

825   hurricane wind analysis system. Journal of Wind Engineering and Industrial

826   Aerodynamics, 77-78: 53-64.

827   Powell, M.D., Vickery, P.J. and Reinhold, T.A., 2003. Reduced drag coefficient for high

828   wind speeds in tropical cyclones. Nature, 422(6929): 279-283.

829   Price, J.F., 1983. Internal wave wake of a moving storm. Part i. Scales, energy budget and

830   observations. Journal of Physical Oceanography, 13(6): 949-965.

831   Price, J.F., Sanford, T.B. and Forristall, G.Z., 1994. Forced stage response to a moving

832   hurricane. Journal of Physical Oceanography, 24(2): 233-260.

833 Rayson, M.D. et al., 2015. Near-inertial ocean response to tropical cyclone forcing on the

834   Australian north-west shelf. Journal of Geophysical Research: Oceans, 120(12):

835   7722-7751.

836 Rimac, A., von Storch, J.-S., Eden, C. and Haak, H., 2013. The influence of high-resolution

837   wind stress field on the power input to near-inertial motions in the ocean.

838   Geophysical Research Letters, 40(18): 4882-4886.

839 Roarty, H. et al., 2010. Operation and application of a regional high-frequency radar

840   network in the mid-atlantic bight. Marine Technology Society Journal, 44(6): 133-

841   145.

842 Roarty, H. et al., 2020. Annual and seasonal surface circulation over the mid-atlantic bight

843   continental shelf derived from a decade of high frequency radar observations.

844   Journal of Geophysical Research: Oceans, 125(11): e2020JC016368.

845 Rodi, W., 1987. Examples of calculation methods for flow and mixing in stratified fluids.

846   Journal of Geophysical Research: Oceans, 92(C5): 5305-5328.

847 Sanford, T.B., Price, J.F. and Girton, J.B., 2011. Upper-ocean response to hurricane frances

848   (2004) observed by profiling em-apex floats. Journal of Physical Oceanography,

849   41(6): 1041-1056.

850 Schofield, O. et al., 2008. The decadal view of the mid-atlantic bight from the coolroom: Is

851   our coastal system changing? Oceanography, 21(4): 108-117.

852 Schofield, O. et al., 2007. Slocum gliders: Robust and ready. Journal of Field Robotics,

853   24(6): 473-485.

854 Schofield, O. et al., 2010. A regional slocum glider network in the Mid-Atlantic Bight

855   leverages broad community engagement. Marine Technology Society Journal, 44(6):

856   185-195.

857 Seroka, G. et al., 2016. Hurricane Irene sensitivity to stratified coastal ocean cooling.

858   Monthly Weather Review, 144(9): 3507-3530.

859 Seroka, G. et al., 2017. Rapid shelf-wide cooling response of a stratified coastal ocean to

hurricanes. Journal of Geophysical Research: Oceans, 122(6): 4845-4867.

Shay, L.K. and Brewster, J.K., 2010. Oceanic heat content variability in the eastern pacific ocean for hurricane intensity forecasting. Monthly Weather Review, 138(6): 2110-2131.

Shchepetkin, A.F. and McWilliams, J.C., 2005. The regional oceanic modeling system (roms): A split-explicit, free-surface, topography-following-coordinate oceanic model. Ocean Modelling, 9(4): 347-404.

Shearman, R.K., 2005. Observations of near-inertial current variability on the new england shelf. Journal of Geophysical Research: Oceans, 110(C2).

Shen, J., Qiu, Y., Zhang, S. and Kuang, F., 2017. Observation of tropical cyclone-induced shallow water currents in taiwan strait. Journal of Geophysical Research: Oceans, 122(6): 5005-5021.

Steiner, A. et al., 2017. Critical weather situations for renewable energies-part a: Cyclone detection for wind power. Renewable Energy, 101: 41-50.

Stommel, H., 2020. The Gulf Stream. University of California Press.

Thiebaut, S. and Vennell, R., 2010. Observation of a fast continental shelf wave generated by a storm impacting newfoundland using wavelet and cross-wavelet analyses. Journal of Physical Oceanography, 40(2): 417-428.

Thyng, K.M. et al., 2021. Performance of offline passive tracer advection in the regional ocean modeling system (roms; v3.6, revision 904). Geoscientific Model Development, 14(1): 391-407.

Toffoli, A., McConochie, J., Ghantous, M., Loffredo, L. and Babanin, A.V., 2012. The effect of wave-induced turbulence on the ocean mixed layer during tropical cyclones: Field observations on the australian north-west shelf. Journal of Geophysical Research: Oceans, 117(C11).

Umlauf, L. and Burchard, H., 2003. A generic length-scale equation for geophysical turbulence models. Journal of Marine Research, 61(2): 235-265.

Vincent, E.M. et al., 2012. Assessing the oceanic control on the amplitude of sea surface

cooling induced by tropical cyclones. Journal of Geophysical Research: Oceans, 117(C5).

Warner, J.C., Defne, Z., Haas, K. and Arango, H.G., 2013. A wetting and drying scheme for roms. Computers & Geosciences, 58: 54-61.

Wu, R., Zhang, H. and Chen, D., 2020. Effect of typhoon kalmaegi (2014) on northern south china sea explored using muti-platform satellite and buoy observations data. Progress in Oceanography, 180: 102218.

Xu, J., Chao, S.-Y., Hood, R.R., Wang, H.V. and Boicourt, W.C., 2002. Assimilating high-resolution salinity data into a model of a partially mixed estuary. Journal of Geophysical Research: Oceans, 107(C7): 11-1-11-14.

Xu, Y. and Yu, X., 2021. Enhanced atmospheric wave boundary layer model for evaluation of wind stress over waters of finite depth. Progress in Oceanography, 198: 102664.

Yang, B., Hou, Y., Hu, P., Liu, Z. and Liu, Y., 2015. Shallow ocean response to tropical cyclones observed on the continental shelf of the northwestern south china sea. Journal of Geophysical Research: Oceans, 120(5): 3817-3836.

Zhai, X., Greatbatch, R.J., Eden, C. and Hibiya, T., 2009. On the loss of wind-induced near-inertial energy to turbulent mixing in the upper ocean. Journal of Physical Oceanography, 39(11): 3040-3045.

Zhang, F., Li, M. and Miles, T., 2018. Generation of near-inertial currents on the Mid-Atlantic Bight by Hurricane Arthur (2014). Journal of Geophysical Research: Oceans, 123(4): 3100-3116.

Zhang, H. et al., 2016. Upper ocean response to Typhoon Kalmaegi (2014). Journal of Geophysical Research: Oceans, 121(8): 6520-6535.